Proceedings World Geothermal Congress 2020+1
Reykjavik, Iceland, April - October 2021

Geomechanical analysis of the hydraulic stimulations in borehole PX2 at Pohang EGS site, South Korea

Andrés Alcolea, Peter M. Meier, Víctor Vilarrasa, Sebastià Olivella and Jesús Carrera

Geo-Energie Suisse AG, Reitergasse 11, CH 8004 Zürich, Switzerland

a.alcolea@geo-energie.ch

Keywords: geomechanics, high-pressure injection, poroelasticity, Pohang earthquake, Enhanced Geothermal System (EGS).

ABSTRACT

A M_w 5.5 earthquake struck the city of Pohang on November 2017, following a sequence of five hydraulic stimulations of an Enhanced Geothermal System (EGS). The triggering mechanism of the mainshock is analyzed by means of a fully coupled hydromechanical model to better understand the behavior of the fault system at the vicinity of the EGS. The results reveal (1) the impact of high injection pressures on the mechanisms triggering seismicity, and (2) the usefulness of hydromechanical modelling for the process understanding and the assessment of seismic risk at any stage of an EGS project.

1. INTRODUCTION

The recent report of the Overseas Research Advisory Committee (ORAC; KGC, 2019) concludes that "the Pohang earthquake was triggered by the EGS stimulation. Seismicity induced by injection activated a previously unmapped fault zone, which in turn triggered the mainshock. Once initiated, the Pohang earthquake grew through the release of tectonic strain. The cuttings extracted during the drilling of PX-2 contained a large amount of fault gouge at depths of about 3,800 m, close to the biggest mud-loss zone, revealing the presence of a fault. The fault's location is close to the intersection with the PX-2 well of the main fault inferred from seismicity. Hydraulic modeling of the injections in PX-1 and PX-2 corroborate the conclusion that the fault responsible for the M_w 5.5 earthquake was stimulated by the PX-2 injection.".

The M_w 5.5 mainshock at the Enhanced Geothermal System (EGS) of Pohang, South Korea, occurred approximately two months after the last injection in borehole PX2. Large-magnitude post-injection seismicity is frequent in EGS activities (see a survey in Evans et al., 2012). However, to the best of our knowledge, a M_w 5.5 event is the largest event triggered by EGS and a delay of 2 months has also no precedent in the context of geothermal activities. In addition to the long-delayed, large-magnitude post-injection seismic activity, the seismicity induced during the stimulations in borehole PX2 is clustered on a steeply dipping plane, termed here "rupture plane", placed some 200 m away from the injection source (KGC, 2019; Bethmann et al, submitted). "Migrated" seismicity far from the injection well is also common in EGS activities (Häring et al., 2008; Dorbath et al., 2009; Deichmann et al., 2014). At Pohang, the rupture plane is the core of a fully developed damage or fault zone (McClure and Horne, 2012). The hypocenter of the mainshock is also located at this plane (KIGAM, 2018; KGC, 2019; Bethmann et al, submitted). This fault zone is placed between the two boreholes that constitute the geothermal doublet, namely PX1 and PX2, and prevents their hydraulic connection because the fault core acts as a hydraulic barrier (Meier et al., submitted). Such fault typology has been reported for faults in southeaster Korea (Choi et al., 2015).

In this work, we aim at gaining understanding on the mechanisms triggering the strong, delayed and migrated seismicity after the EGS stimulation at Pohang by using a fully coupled hydromechanical numerical model including poroelastic effects. The model is first calibrated using measurements of hydraulic stimulations PX2-1 and PX2-2. Second, a simulation of PX2-3 is done, which allows to estimate the hydromechanical regime at the time of the mainshock. Unfortunately, the authors have not had access to the raw data acquired during PX2-3. Thus, the simulation is based on soft (though reliable) information. The calibrated model is used to predict the hydromechanical regimes and assess the potential seismicity in scenarios in which the maximum injection pressure is limited to 30 MPa (similar to that in the Basel EGS, Häring et al., 2008) and 10 MPa (the maximum allowed by the French regulations in e.g., Soultz-sous-Forêts; Gerard et al., 2006). The conclusions of this study are important for future EGS projects, especially when critically stressed faults are present in the project area, like in Pohang.

2. OVERVIEW OF THE POHANG EGS PROJECT

The high geothermal gradient in the area near Pohang (41°C/km vs. a mean 25°C/km in South Korea; Kim et al., 2018; Lee et al., 2010 and 2015) motivated the selection of Pohang for the deep geothermal project. The deep granodioritic reservoir (with top at ~2200 m depth) is overlaid by ~1400 m of Tertiary mudstone and Cretaceous sandstone/mudstone, and by a shallow layer of ~800 m of Cretaceous volcanic rocks (Son et al., 2015; Zingg et al., submitted). The EGS consists of two boreholes, namely PX1 and PX2 While PX1 is side-tracked to the WNW and reaches a measured depth of 4215 m, PX2 is pseudo-vertical to a measured depth of 4348 m. The open-hole sections of PX1 and PX2 start at a depth of 4215 m and 4208 m, respectively.

During the drilling of PX2, massive mud-losses occurred at depths below ~3830 m (KGC, 2019). This depth coincides with the location of the fault (KGC, 2019). A 30% of fault gouge was found at this depth (KGC, 2019; Zingg et al., submitted). This layer is associated with a low permeable fault core that is surrounded by medium- to high-permeability layers. The low permeability of the fault core is also confirmed by the interpretation of the hydraulic data measured during the first hydraulic stimulation in PX1, which reveals the presence of an "impermeable barrier" (actually very low-permeable), detected by the doubling of the slope of the curve overpressure vs time in a semi-log plot of (Meier et al., submitted). Furthermore, this depth coincides with the intersection between borehole PX2 and the plane that best fits the seismicity associated with the three stimulations in borehole PX2 and the sequence of foreshocks and the M_w 5.5 mainshock on November 2017. The fact that this fault core was the rupture plane was confirmed when the

logging wireline was unable to go deeper than 3823 m during the logging attempt in borehole PX2 in August 2018 (KGC, 2019). This is attributed to an obstruction in the borehole, which was likely damaged by the slip caused by the mainshock.

Overall, five alternate hydraulic stimulations in boreholes PX1 and PX2 were carried out between February 2016 and August 2017. According to KGC (2019), 12798 m^3 of water were injected (5663 m^3 in PX1 -second and fourth stimulations- and 7135 m^3 in PX2) and 6957 m^3 were flowed back (3968 and 2989 m^3 from PX1 and PX2, respectively). The maximum overpressures in PX2 were close to 90 MPa during the three stimulations. The maximum flow rate was 47 L/s during PX2-1. In contrast, the maximum overpressures in the PX1 stimulations were way lower, up to 28 MPa with a maximum flow rate of 18 L/s during PX1-1 (the second stimulation in the sequence of five). The fact that these two close boreholes react to injection in a so different manner, and the substantially different seismic sequences during and after the stimulations of PX1 and PX2, are additional evidences for the existence of different hydrogeological and mechanical regimes separated by a fault zone.

3. THE HYDROMECHANICAL MODEL

We reproduce the hydromechanical response of the system to the sequence of three high-pressure injections in borehole PX2 by using a fully coupled hydromechanical model. Neglecting the injections in PX1 allows us to simplify the problem to 2D plane strain conditions by assuming that the layers defining the fault zone present long continuity in the direction orthogonal to the plane of the model (Figure 1). Thermal effects caused by the cooling of the system after the injection of "cold" water (at ~60° at the depth of the inflow source) have been neglected because the volume of cooled rock is negligible for the small amounts of injected water during EGS stimulations and thus, they are relevant only close to the inflow source (De Simone et al., 2013 and 2017, among others). The coupling of hydraulic and mechanical phenomena is solved using the software Code_Bright, a finite element method code that solves the hydromechanical coupling in a fully coupled way (Olivella et al., 1994 and 1996).

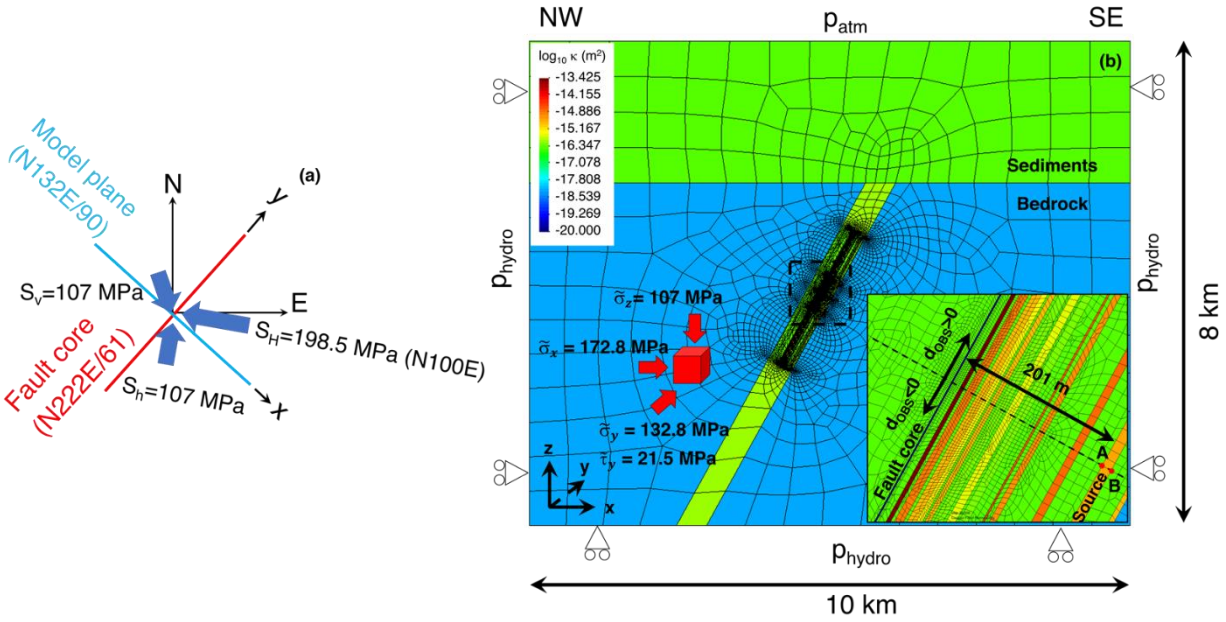

Figure 1: (a) Aerial view of the model setup and principal components of the stress tensor defining the preferred stress state at 4.2 km depth (following the sign criterion of geomechanics, compression positive; Castilla et al., submitted). The model plane is vertical and orthogonal to the plane of the fault core (termed here indistinctly "rupture plane"); (b) cross section showing the model plane (y axis positive from SSW to NNE and parallel to the rupture plane) and spatial distribution of log-permeability prior to the hydraulic stimulation. The arrows depict the rotated stress state in the plane of the model. The inset zooms at the fault zone between the layers were water was injected (termed here "source layer") and where seismicity was monitored (i.e., the rupture plane). Points A and B are the points where the boundary conditions at the source are implemented. d_{OBS} denotes the distance along the rupture plane from the point closest to the inflow (termed here "central point"; positive d_{OBS} upwards along dip). Results will be displayed at control points along such axis.

The model plane is vertical (N132E/90; Figure 1a) and orthogonal to the rupture plane. In this work, we have chosen an orientation N222E/61 (Figure 1a) that corresponds to an early estimate made by the Korean Institute of Geoscience and Mineral Resources (Figure 13 in KIGAM, 2018) in June 2018, when we built our numerical model. Alternative reported orientations are N204-N205E/43-58 (KGC, 2019), N225E/66-75 (Grigoli et al., 2018) and N227E/50 (Bethmann et al., submitted). The fault zone is composed by forty layers. In the absence of further information on the dip of the different layers, all of them have been assumed to be parallel (inset in Figure 1b). Layer-wise heterogeneous distributions of the main mechanical (Young's modulus and Poisson ratio) and hydraulic parameters (permeability and specific storage) have been assigned from available data sets or published works (Dahm et al., 2018; Yoo et al. 2017, 2018; KIGAM, 2018; KGC, 2019) and are not presented here for the sake of brevity. Other model parameters (e.g., fluid viscosity, solid density, etc.) have been inherited from previous works or are standard in scientific literature.

The rupture plane is assumed to be cohesionless, as suggested by the high fault gouge content. The friction coefficient, ψ, at the rupture plane is, as usual, highly uncertain. A value of ψ ~1.66 (core at 4220 m depth; Kwon et al. 2019) has been reported for the

intact rock and a value in the range of ψ ~0.54-0.68 (cuttings at 3607 m in PX-2, above the rupture plane; KGC, 2019) for the fault. A preliminary analysis of Coulomb Failure Stress (CFS=$|\tau|$-(c+$\psi\sigma'_n$), where c is cohesion τ and σ'_n are shear and normal effective stress, respectively) suggests friction coefficients for the rupture plane, ψ_{RP}, ranging from 0.4 to 0.45. Such relatively low values are common in clay-rich faults (Reasenberg and Simpson, 1992; Iio, 1997; Tanikawa and Shimamoto, 2009; Barth et al., 2013). In view of the large uncertainties, the friction coefficient at the rupture plane in our model is inferred in such a way that the model calculates unstable conditions ($CFS \geq 0$) at the rupture plane and at the timestamps of monitored seismic events, resulting in ψ_{RP} =0.425.

The local stress state has been analyzed by different authors using different methods and data sets, resulting in a manifold of possible stress states. The used methods include hydraulic fracturing in shallow boreholes, focal mechanisms and well-logs. The estimated state of stress gives either strike-slip, transitional between strike-slip and reverse-faulting, or reverse-faulting conditions. We have chosen for our model a transitional stress state between strike-slip and reverse faulting (Figure 1; Castilla et al., submitted). To cope with uncertainties, a comprehensive and thorough sensitivity analysis of model inputs to, e.g., the native stress state, the friction coefficient and the permeability of the rupture plane, was carried out (Alcolea et al., submitted) and is omitted here for the sake of brevity.

Hydromechanical boundary conditions (Figure 1b) are (1) free displacement and atmospheric pressure on top, (2) zero lateral displacement and hydrostatic pressure along NW and SE laterals, and (3) zero vertical displacement and no flow on bottom. The inflow is concentrated at the two nodes at the top of the openhole section, tagged as A and B in Figure 1b. In the absence of more detailed information, the source layer containing nodes A and B is assumed to be parallel to the rupture plane. This inclination may not be coherent with some of the plausible stress states, i.e., the source layer may be even horizontal in a reverse-faulting stress regime. In such case, the distances between the injection-induced pressure front and the rupture plane would be smaller, thus facilitating seismicity at the rupture plane during and at early times after injection. Therefore, the geometry of our model represents a worst-case scenario.

Boundary conditions at nodes A and B are either a prescribed fluid mass flux (during injection periods), zero mass flux (shut-in), or hydrostatic pressure (bleed-off) boundary conditions. In our 2D model, mass fluxes are defined per unit width, W, in the off-plane direction. W represents the length along which the fluid enters the system. As such, W depends on the injection history. The mass flux at nodes A and B (Figure 1b) is $m_{A,B}$=0.5 Q ρ_0 / W, where ρ_0 is the density of the incoming fluid and both Q and W vary with time. As expected, if the actual injected fluid mass $Q\rho_0$ is implemented without the width correction, the calculated overpressure at the inflow points is ~50 times larger than the measured wellhead pressure because the plane strain model assumes a thickness of 1 m. The wellhead pressure is assumed to be equal to the downhole overpressure, i.e., friction losses along the tubing are neglected for simplicity.

Besides variations in model width, the injection causes a severe and cyclical deformation of the source layer (expansion and shrinking during injection and shut-in/bleed-off periods, respectively) that varies its permeability κ_{SL} and stiffness E_{SL} (note that the porosity variations are automatically calculated by the simulator Code_Bright to accommodate volumetric deformations). Correspondingly, W, κ_{SL} and E_{SL} are calibrated against measured wellhead pressures from hydraulic stimulations PX2-1 and PX2-2. Provided that the authors of this work have not been granted access to the raw data set, data of PX2-3 have been digitized from the recently published KGC (2019) report. Thus, hydraulic data sets from PX2-3 are not used for calibration, but for prognose. For simplicity, we assume that the permeability and the stiffness of the remaining layers do not vary in time. The impact of this hypothesis in the rupture plane is low because the distance to the source layer is large. Finally, initial conditions are lithostatic and hydrostatic, i.e., coherent with the hydromechanical boundary conditions.

The mesh is composed by quadrilateral elements, with refinement at the fault zone, resulting in 14'066 elements (Figure 1b). Each injection/shut-in/bleed-off cycle has been modelled as a separate time interval. The temporal discretization varies depending on the convergence rate of the Newton-Raphson's algorithm for solving the non-linearities caused by the coupling of hydraulic and mechanical phenomena (Milly, 1984). The initial time step in each interval has been set to 10^{-4} days and no restrictions apply to the minimum and maximum time steps. Model parameters W, κ_{SL} and E_{SL} have been calibrated at each time interval.

4. RESULTS

Figure 2 presents the temporal evolution of the calibrated permeability of the source layer, κ_{SL}, and of the model width W used to adapt the actually injected mass flux to plane strain conditions. Two observations become apparent during the calibration periods PX2-1 and PX2-2 (the first two columns in Figure 2). First, κ_{SL} displays a cyclic character that resembles well that of the generated overpressure (Figures 2g and h), i.e., κ_{SL} increases during injection periods and decreases during shut-in/bleed-off periods. As observed, little gain in terms of permeability is achieved after PX2-1 and/or PX2-2. Actually, the permeability gain is almost reversible, which suggests a cycling opening and closing of fractures rather than the expected hydro-shearing fracture with permanent permeability gain (or, overall, transmissivity) in igneous rocks (see a survey in Evans et al., 2012). Yoo et al. (2017) and Yoo (2018) got to the same conclusion using a pseudo-homogenous 3D hydromechanical model. Similarly, Min et al. (2017) report sharp and cyclic variations of κ_{SL} by analyzing hydraulic data, i.e., neglecting the coupling with mechanical effects.

Second, the model width W increases rapidly after the first few injection cycles of PX2-1 and remains approximately constant afterwards, increasing by a factor of 2 during the longest injection cycles of PX2-2. This response will be further explored below. Note that W only intervenes in the calculations during the injection periods, i.e., when the injection mass flux is not zero. For the prognose of PX2-3, given the lack of actual data, the source layer is attributed with two permeability values (Figure 2c), κ_{SL} =2.90·10^{-16} m^2 and κ_{SL} =8.75·10^{-17} m^2 during injection and shut-in/bleed-off periods, respectively. Additionally, W (Figure 2f) varies with time in such a way that the calculated overpressure at the source layer (1) does not exceed 90 MPa, and (2) reproduces the available "soft information" digitized from KGC (2019). The Young's modulus of the source layer, E_{SL}, was also calibrated (not shown here for the sake of conciseness). A progressive softening of the source layer is observed from the initial value of 36.4 GPa to a final value of 3.4

GPa, which is achieved only after 0.115 days of stimulation PX2-1, coinciding with the first peak in injection overpressure at the source layer, Δp_{SL}~67.5 MPa.

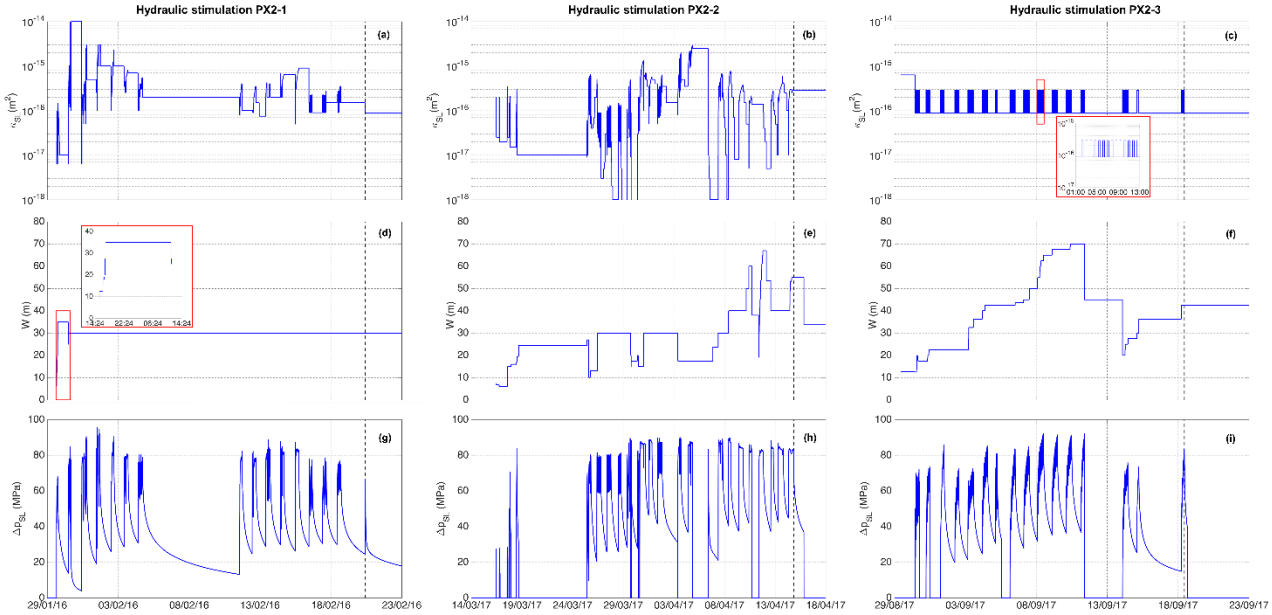

Figure 2: Temporal evolution of model parameters: (a to c) permeability of the source layer κ_{SL}; (d to f) off-plane model width *W*; (g to i) calculated overpressure at the source layer as a reference. Vertical dashed lines represent the end of each hydraulic stimulation. Note that κ_{SL} and *W* were calibrated for stimulations PX2-1 and PX2-2 only (left and middle columns, respectively). Instead, κ_{SL} was assigned for the prognose of PX2-3 (panel c). Two values were used during injection ($\kappa_{SL}=2.90\cdot10^{-16}$ m^2) and shut-in/bleed-off cycles ($\kappa_{SL}=8.75\cdot10^{-17}$ m^2). The off-plane model width (panel f) varies with time in such a way that the calculated overpressure at the source layer (1) does not exceed 90 MPa, and (2) resembles the "soft information" digitized from KGC (2019).

Figure 3 displays the calculated and measured overpressure at the source layer. Overall, the calibration is satisfactory, as shown by the normally distributed (not reported here) calibration residuals *r*, i.e., calculated minus measured overpressure, and by their overall small statistics, i.e., $\langle r \rangle$ = -0.12 MPa and σ_r= 2.86 MPa (0.13% and 3.1 % of the maximum measured overpressure, respectively). Obviously, different combinations of calibrated parameters values (especially κ_{SL} and *W*) may lead to similar results because the calibration problem is ill-posed (Carrera et al., 2005). However, we argue that, despite model uncertainties and ill-posedness, the calibrated parameters are plausible because the permeability of the source layer (1) is typical of crystalline fractured reservoirs at a depth of ~4 km (Stober, 2011; Stober and Bucher, 2007 and 2015; Evans et al., 2012), and (2) its temporal evolution resembles well that in Yoo (2018). In addition, the variation of κ_{SL} with overpressure (not displayed here) compares well with that obtained by conventional interpretation methods involving data deconvolution (Birsoy and Summers, 1980) and purely hydraulic analytical solutions (e.g., Theis, 1935) using the open source software HYTOOL (Renard, 2017).

Figure 4 displays the hydromechanical impact caused by injection at the end of the three stimulations and at the time of the mainshock. Three phenomena occur simultaneously at the rupture plane: (1) a destabilizing pressure build-up, which reduces the effective stresses ($\Delta p > 0$), (2) a stabilizing mechanical compression during injection of the rock surrounding the source layer, i.e., an upward "push" of the overall fault zone to the upper left part of the model caused by the injection-induced expansion of the source layer ($\Delta\sigma_n>0$; note that this effect vanishes during shut-in and bleed-off periods), and (3) a destabilizing increment of shear stress during injection resulting from the anisotropic changes in total stresses ($\Delta\tau>0$). Note that there is a competition between the increases in normal stress and pore pressure to determine whether the resulting variation in effective normal stress ($\Delta\sigma'_n=\Delta\sigma_n-\Delta p$) is positive (stabilization) or negative (destabilization).

Figure 4 shows that the spatial distribution of overpressure is elliptical and not radial away from the inflow (Figures 4a to d), which is caused by the heterogeneous distribution of permeability in the fault zone (i.e., a sequence of interbedding layers alternating high and low permeability; Figure 1b) and by the low permeability of the rupture plane, which acts as a "barrier" to fluid flow (Meier et al., submitted). A 2500 m-long patch along the rupture plane suffers from overpressures in the range of 2 to 3 MPa after the stimulations, and of ~2 MPa at the time of the mainshock. Fluid injection "pushes" the fault zone upwards, towards the upper left corner of the model, which compresses the rupture plane during injection. This compression contributes to its stabilization of the rupture plane because the normal stress to the plane increases, which tends to close it (Figures 4e to h). During shut-in and bleed-off periods, the source layer shrinks, removing the injection-induced stabilization effect (i.e., the compression) at the rupture plane. This vanishing of the fault compression explains the delayed seismicity after stimulation, as can be observed in Figures 4i to 4l, which represent the combination of mechanical compression and pressure build-up in terms of variation of effective normal stress. Overall, the dominant phenomenon is pressure build-up, which leads to a reduction in the effective normal stress $\Delta\sigma'_n$.

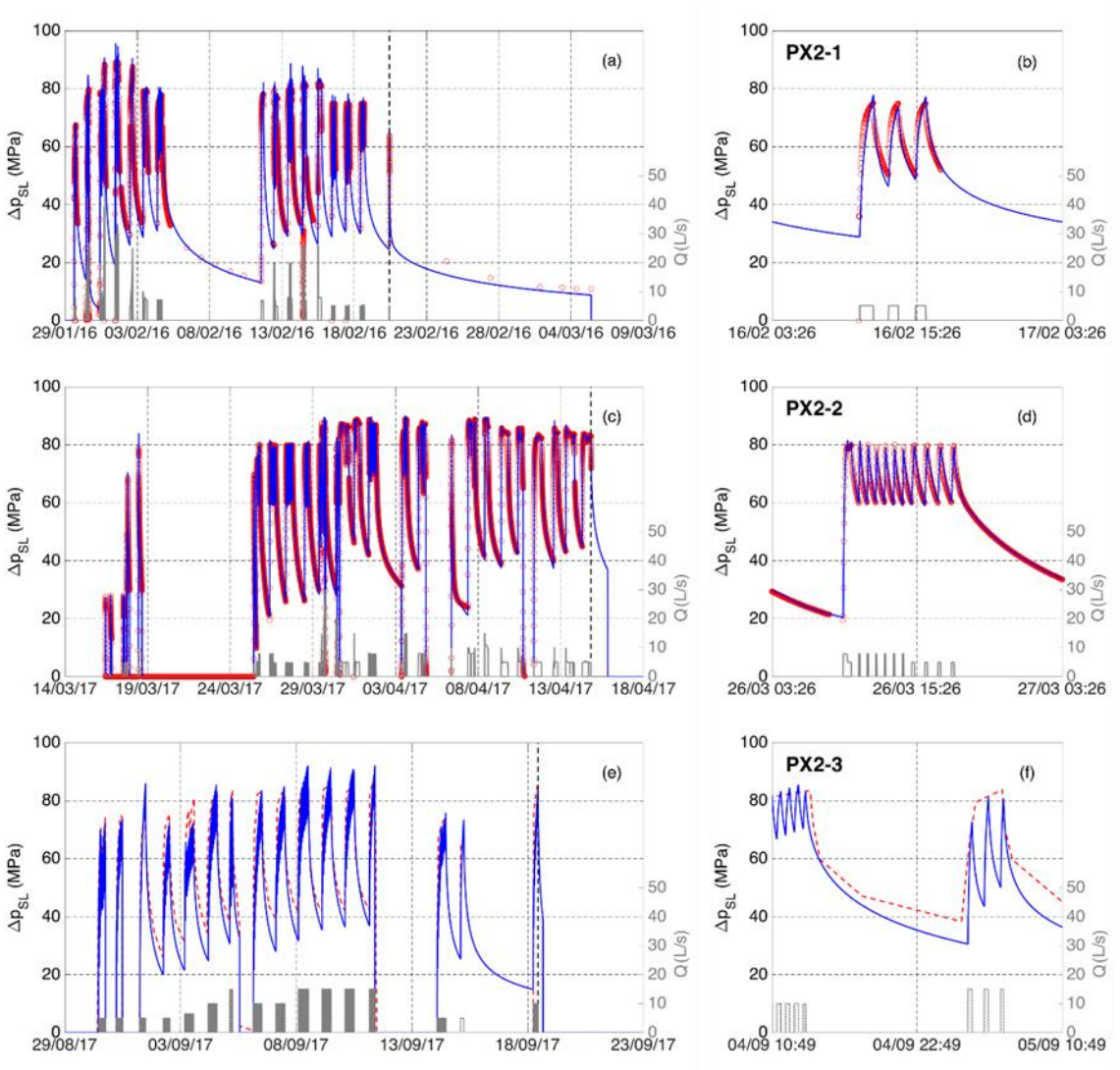

Figure 3: Calculated and measured overpressures at the source layer and injection flow rates during hydraulic stimulations PX2-1 (panels a and b), PX2-2 (c and d) and PX2-3 (e and f). Panels b, d and f are zooms to selected 1-day periods. Calculated and measured overpressures are depicted by solid blue lines and red circles, respectively, except for PX2-3 (dashed red line representing soft information digitized from KGC, 2019). Grey lines depict the measured injection flow rates (Q, associated with the right axis). Vertical dashed lines represent the end of each hydraulic stimulation.

The final effect is the positive increment of shear stress along a long patch of the rupture plane during injection, which tends to destabilize (Figures 4m to 4o). The pressure build-up caused during injection compresses the rock, which induces an increase in the horizontal total stresses because of the lateral confinement (e.g., Segall and Fitzgerald, 1998). Since the vertical total stress remains practically unaltered, the deviatoric stress increases in a transitional stress regime because the maximum principal stress is horizontal, and the minimum is vertical and identical to the horizontal minimum stress. The situation is reversed after shut-in (note the negative variation of normal stress at the time of the mainshock (Figure 4h), which causes a reduction in the horizontal total stress and thus, of the deviatoric stress, but with smaller magnitudes, leading to a slight increase in stability). Thus, assessing fault stability is not trivial because shear stress and effective normal stress have opposite effects. The assessment of the stability of the rupture plane can be performed taking into account these competing effects by analyzing *CFS* (Figure 5). Figure 6 plots the variations of overpressure, normal, effective normal and shear stresses along the central part of the rupture plane (note that only the central 2000 m are shown to better display the effects at short distances from the source layer; see also Figure 4).

The variations are either symmetric (pressure and shear stress) or antisymmetric ($\Delta\sigma_n$ and $\Delta\sigma'_n$) with respect to an axis orthogonal to the fault zone at d_{OBS}~0, where the hydromechanical effect is the strongest. As observed, a 800 m-long patch along the rupture plane suffers from overpressures of more than 2 MPa (Figure 5a) and 2500 m are affected by positive overpressures regardless of the stimulation scheme. An overpressure of 2 MPa persists long after the end of the last hydraulic stimulation PX2-3, extending until the time of the mainshock. Actually, pressure diffusion after the cease of the last injection equalizes pressure to 1.8-2 MPa along the 2500 m-long patch. Although the patch is compressed along its whole length ($\Delta\sigma_n$ >0, which contributes to stabilization; Figure 5b), pressure build-up dominates and, overall, the effective normal stress is reduced (Figure 5c), especially along the upper part of the patch (d_{OBS}>0), where normal stresses are lower. At the end of the stimulations, while the upper part of the patch suffers from a reduction in the effective normal stress of 2.0 to 3.0 MPa, the reduction along the lower part of the patch is only of 0.5 to 1.0 MPa. The largest reduction in the effective normal stress (~2.8 MPa) is observed at the upper part of the patch and at the end of PX2-2,

which may explain the M_w 3.1 that occurred right after the cease of injection. At the time of the mainshock, there is still an overall reduction in the effective normal stress of 0.8 to 1.5 MPa, with lower values along the lower part of the patch (d_{OBS}<0). The variation of shear stress (Figure 5d) at the time of the mainshock is negative (overall reduction of 0.2-0.5 MPa), which tends to slightly stabilize the rupture plane. This is not the case during the stimulations, where shear stresses increase 0.5 to 1.0 MPa along a length of ~400 m near the central part of the patch, which favors instability. However, since the changes in shear stress are smaller than those in effective normal stress, shear stress variations have a smaller effect than variations in the effective normal stress on the stability of the rupture plane.

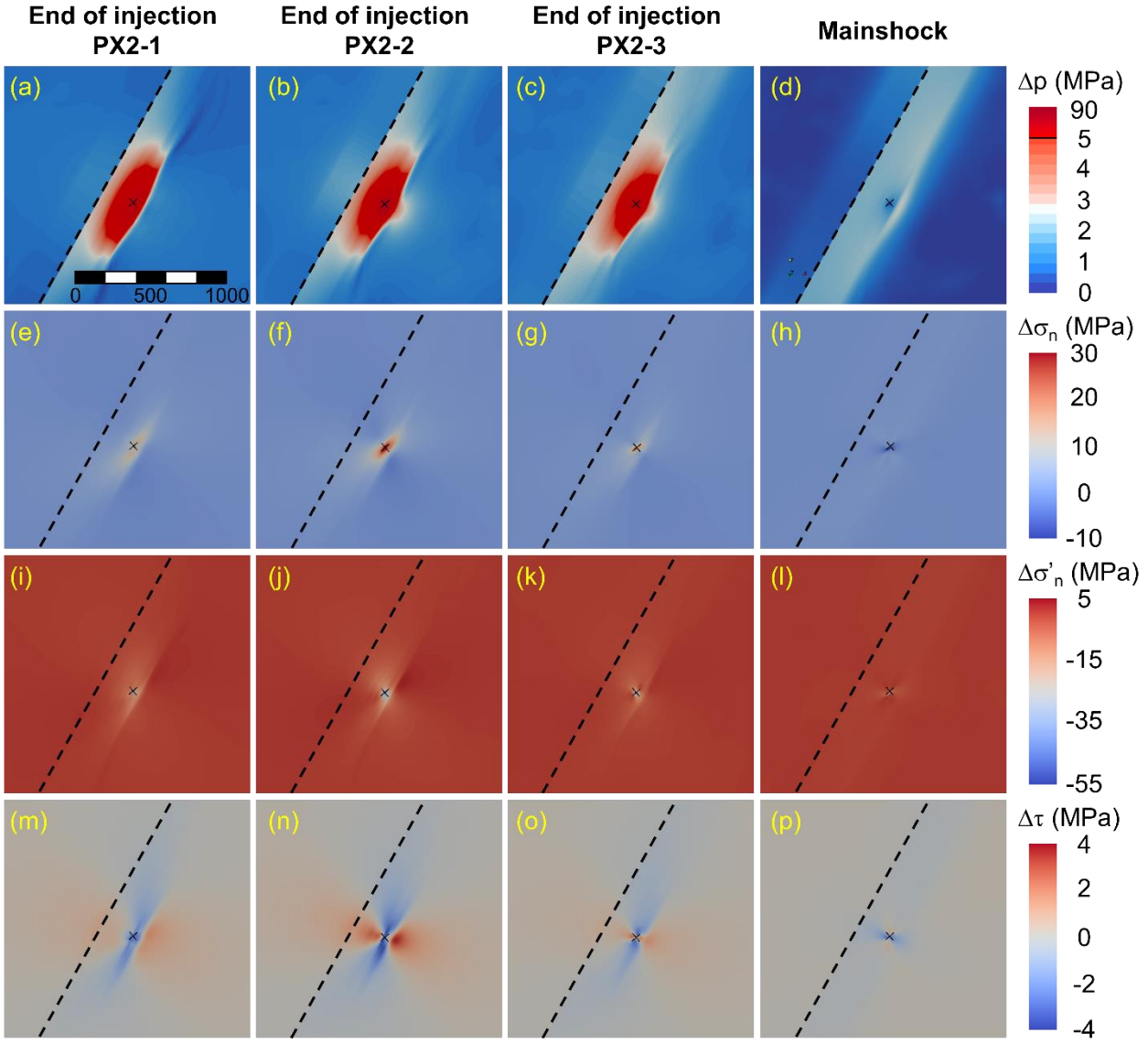

Figure 4: Contours of overpressure Δp (a to d), and of variations of normal stress $\Delta\sigma_n$ (e to h), effective normal stress $\Delta\sigma'_n$ (i to l) and shear stress $\Delta\tau$ (m to p) at the end of hydraulic stimulations PX2-1, PX2-2, PX2-3, and at the time of the mainshock (columns). Normal and shear stresses are calculated at the rupture plane N222E/61. Positive incremental normal stress means more compression. The source is depicted by a cross and the rupture plane by a dashed black line. Note that the color scale of Δp (panels a to d) is truncated at Δp=5 MPa to better display the lowest values.

The variations of effective normal and shear stress control the stability of the rupture plane, which also depends on friction. We use a "base case" friction coefficient ψ_{RP}=0.425 to calculate ΔCFS. ΔCFS measures the amount of stabilization/destabilization with respect to the initial state, with negative values indicating stabilization (Figure 5e). Such friction coefficient leads to unstable conditions at the rupture plane at the timestamps of monitored seismic events (see Figure 6 and the corresponding discussion below), including the mainshock. Thus, according to our results, no hardening or weakening, i.e., rate-and-state friction (Noda, 2013; Tanikawa and Shimamoto, 2009), occurred at the rupture plane. As observed, the 2500 m-long patch tends to destabilize (ΔCFS >0) at the end of the three stimulations and at the time of the mainshock. Figure 5f shows that the CFS is positive along a length of 800-1500 m at the end of each hydraulic stimulation and that this unstable patch is centered at d_{OBS}~0. In contrast, the lower and upper parts of the rupture plane are stable. After the cease of the last injection, pressure diffuses and increases along the lower and upper parts of the rupture plane (and decreases at its center; Figure 5a), which reduces effective normal stresses (pseudo-flat blue curve in Figure 5c). This reduction, combined with that of shear stresses in the same areas (Figure 5d), destabilizes a 2500 m-long patch

(pseudo-flat blue line in Figure 5f). The maximum *CFS* is located at d_{OBS}~-1000 m, i.e., at the lower part of the rupture plane, where the mainshock was located. It is precisely the flat pressure profile in Figure 5a (blue line) what may explain the long delay of 2 months between the end of the last stimulation and the mainshock, i.e., as pressure diffuses, longer sections become unstable.

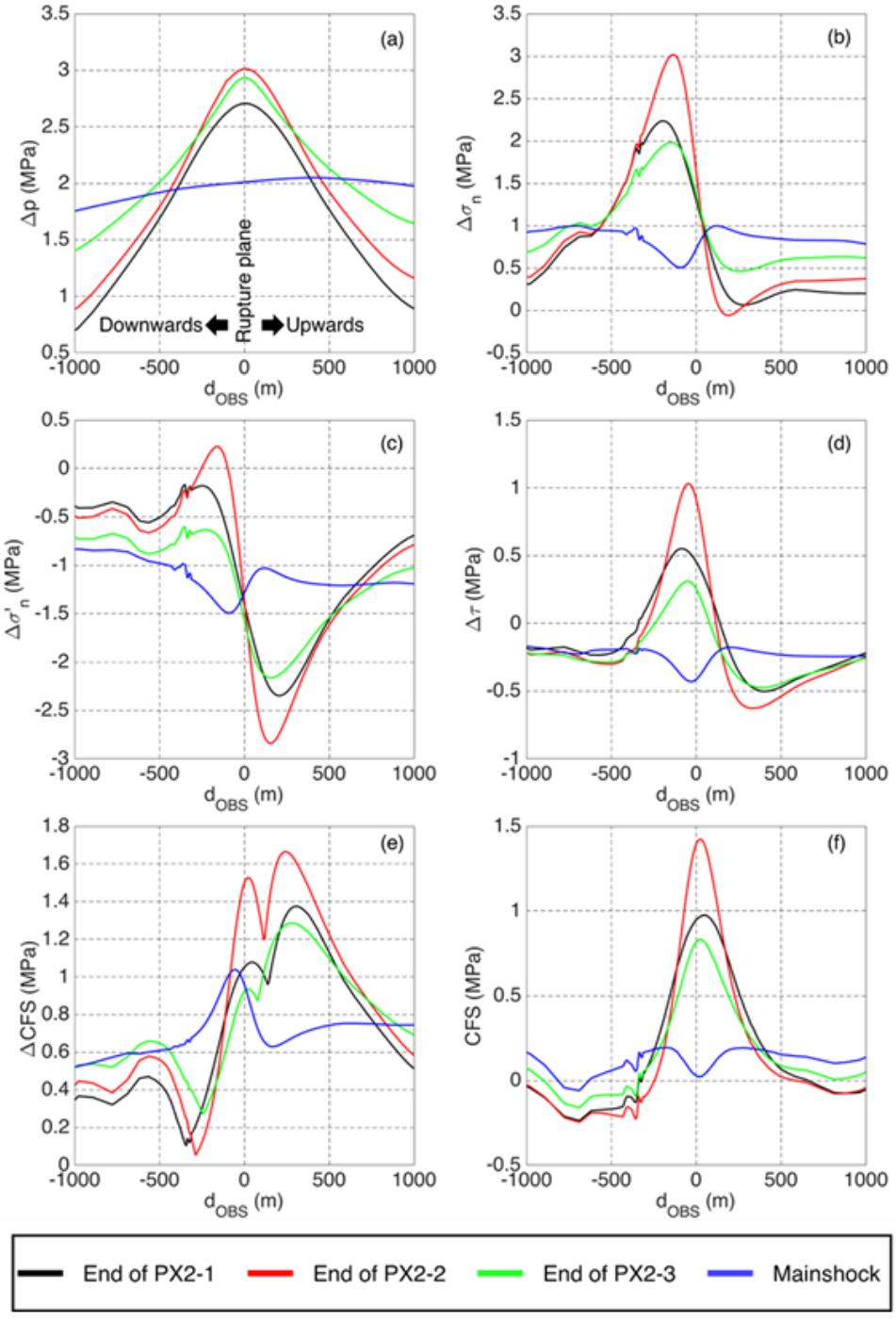

Figure 5: Spatial distribution along the rupture plane of (a) overpressure, (b) variation of normal stress, (c) variation of effective normal stress, (d) variation of shear stress, (e) variation of CFS and (f) CFS. Normal and shear stresses are calculated at a plane N222E/61. Positive variations of normal stress mean more compression. The local coordinate system d_{OBS} is displayed in Figure 1b.

Figure 6 displays the spatio-temporal evolution of the stability/instability conditions at the rupture plane in terms of *CFS*, which accounts for all hydromechanical effects together, at different control points. As soon as the first stimulation commences (Figure 6b), *CFS* becomes positive (meaning instability) at the rupture plane, coinciding with the timestamp of the first monitored events at the rupture plane (blue dots and crosses in Figure 6). Regardless of the hydraulic stimulation (Figures 6b to 6d), *CFS* increases during injection and decreases during shut-in and bleed-off periods. The peaks in the *CFS* curves are caused by purely mechanical undrained effects and resemble well and almost without delay the response at the rupture plane in terms of overpressure. In terms of *CFS*, the region close to the injection well ($|d_{OBS}|\leq$50 m, not displayed in Figure 6 because the *CFS* curves are nearly identical to that at d_{OBS}=0 m) responds rapidly to pressure changes, both during injection and after shut-in. Nevertheless, an increasing delay for increasing

distances along the rupture plane is observed, which even yields enhanced stability conditions at early times of injection and stability reduction after shut-in for $|d_{OBS}|$>200 m. Overall, an increasing trend is observed during stimulation periods, whose slope mainly depends on the injected volume during each hydraulic stimulation and on the stimulation scheme, i.e., the way that volume was injected.

Regardless of the hydraulic stimulation and of the distance along the rupture plane, *CFS* tends to progressively recover the initial values after the last injection period, i.e., the rupture plane stabilizes again, with the exception of PX2-3 because the recovery time of ~4.5 months after PX2-2 was not long enough. During PX2-1 (Figure 6b), a total volume of 1970 m^3 was injected during 22 days using long stimulation periods of about 6 hours, with embedded shut-in periods (notably, one of about 1 week after the sixth day of stimulation) and almost without bleed-off (overall, only 181 m^3). The injection scheme was seemingly homogeneous in time, which leads also to homogeneity of the temporal sequence of seismicity during injection. The frequency of monitored seismic events increased, as usual, after the last cease of injection (e.g., Häring et al., 2008; Deichmann and Giardini, 2009; Evans et al., 2012, among others). The largest event magnitude during PX2-1, M_L=1.4, occurred four days after shut-in. The model reproduces consistently unstable conditions (*CFS* ≥ 0) during stimulation at a ~2500 m-long patch along the rupture plane more than 10 months after the cease of injection (see also Figure 7). In fact, a series of seismic events were monitored and located at the rupture plane (Bethmann et al., submitted) between 17/12/2016 and 31/12/2016. At that period, the model successfully forecasts unstable conditions at the lower part of the rupture plane (d_{OBS}=-200 m and d_{OBS}=-1000 m; Figure 6a).

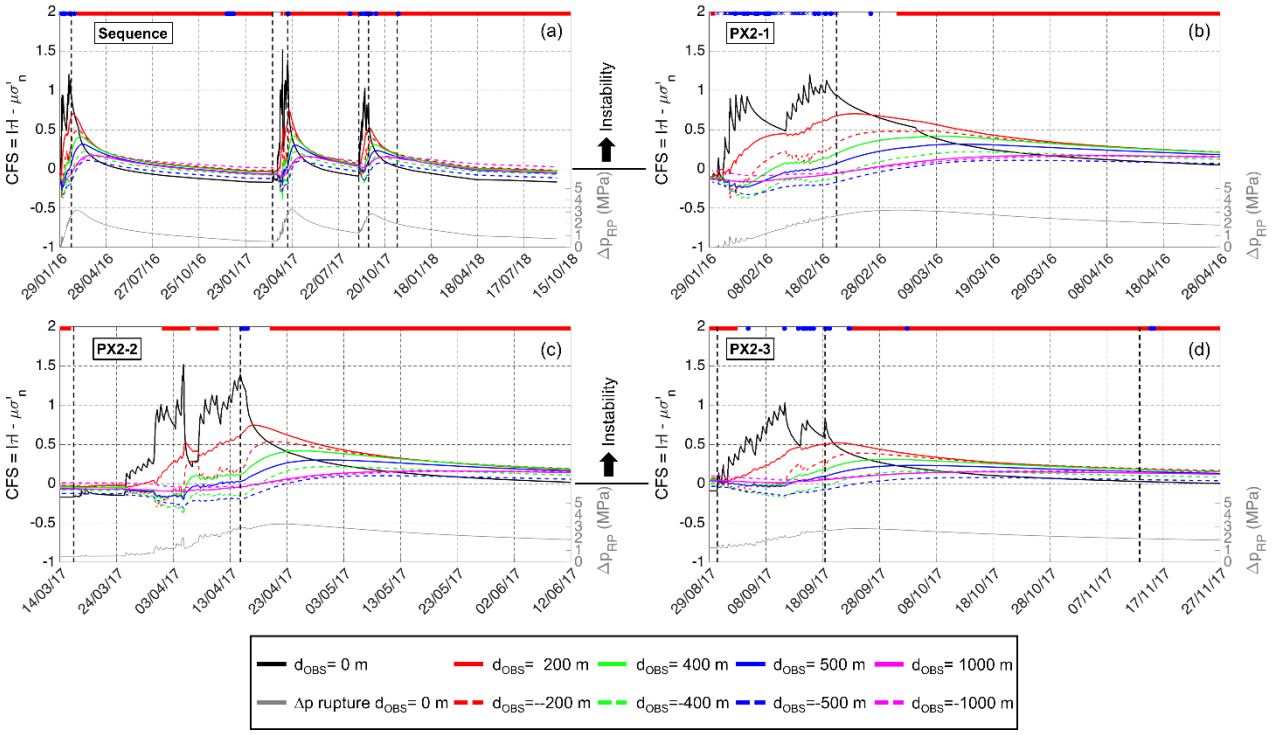

Figure 6: Temporal evolution of Coulomb failure stress, *CFS*, at control points along the rupture plane: (a) complete sequence of hydraulic stimulations in borehole PX2, (b to d) zoom to individual hydraulic stimulations PX2-1, PX2-2 and PX2-3. The vertical dashed lines depict the beginning and end of the stimulation periods and the timestamp of the mainshock. Blue circles and crosses depict the timestamp of the monitored seismic events (blue circles: interpretation by Geo-Energie Suisse AG, Bethmann et al., submitted; blue crosses: digitized from KGC, 2019). The red patches on top depict the time periods during which the monitoring seismic network was incomplete or not installed. The grey lines, associated with the right vertical axis, depict the temporal evolution of overpressure at control point d_{OBS}=0 m.

In contrast to PX2-1, 2828 m^3 of water were injected during 30 days during PX2-2, but using short 5-minutes injection periods followed by similar shut-in or bleed-off periods. Overall, 1218 m^3 were bled, 7 times more than during PX2-1. Only during the last ten days of stimulation, the first concept of long stimulation periods was recovered. The impact of the stimulation scheme at early times is translated into a delay of more than 10 days in the hydromechanical response at the rupture plane (Figure 6c). The change in the slope of *CFS* on 30/03/2017 approximately coincides with the first long injection cycles. The maximum value *CFS*=1.5 was attained on 6/4/2017, during a period when the seismic monitoring network was not operative (red patches in Figure 6). The maximum event magnitudes, i.e., M_L=3.1 and 2.0, were recorded soon after the cease of injection. Two seismic events were monitored and located near the rupture plane on 13/08/2017. Again, the model successfully forecasts unstable conditions at the corresponding timestamps and during a long period of 4.5 months after the cease of injection at distances from the center of the rupture $|d_{OBS}|$>200 m. However, the size of the unstable patch did not increase further during this stimulation (Figure 7).

During the last hydraulic stimulation, PX2-3 (Figure 6d), 2256 m^3 of water were injected during 19 days, and 1228 m^3 were bled. Unfortunately, the authors did not have access to the history of monitored flow rates and wellhead pressures. However, it is known that the injection scheme was similar to that of PX2-2. For the prognose, an estimation of the injected flow rate has been made by applying the features of the stimulation PX2-2 and the reported injected and bled volumes. Correspondingly, the hydromechanical

responses at the rupture plane are similar during PX2-2 and PX2-3 (but for the absence of delayed response in PX2-3, likely caused by the already unstable state of the rupture plane prior to injection). The maximum event magnitude, again shortly after the cease of injection, was M_L=1.8. Once again, the model consistently forecasts unstable conditions during injection, shut-in and until August 2018, long after the mainshock (Figure 6d). At that date, the length of the unstable patch, which did not increase during the third hydraulic stimulation, is ~2500 m.

Figure 7 presents the temporal evolution of the maximum accumulated length of the unstable patch. Unfortunately, the dimensionality of the model precludes the extrapolation of unstable length to rupture area (and ultimately to event magnitude by applying scaling relations, e.g., Eshelby, 1957; Lay and Wallace, 1995). The first hydraulic stimulation, PX2-1, already destabilized a 1000 m-long patch at the cease of injection. The patch grows with time during the period between the first and second hydraulic stimulations, up to a maximum length of 2.5 km, a plateau that was attained on 30/03/2016, only 62 days after PX2-1 began. During the second and third stimulations, the applied stimulation schemes involving short stimulation cycles cause indeed unstable conditions at the rupture plane (*CFS*≥0 in Figures 6c and 6d), but at a portion of the patch that already reached unstable conditions during or after the first hydraulic stimulation.

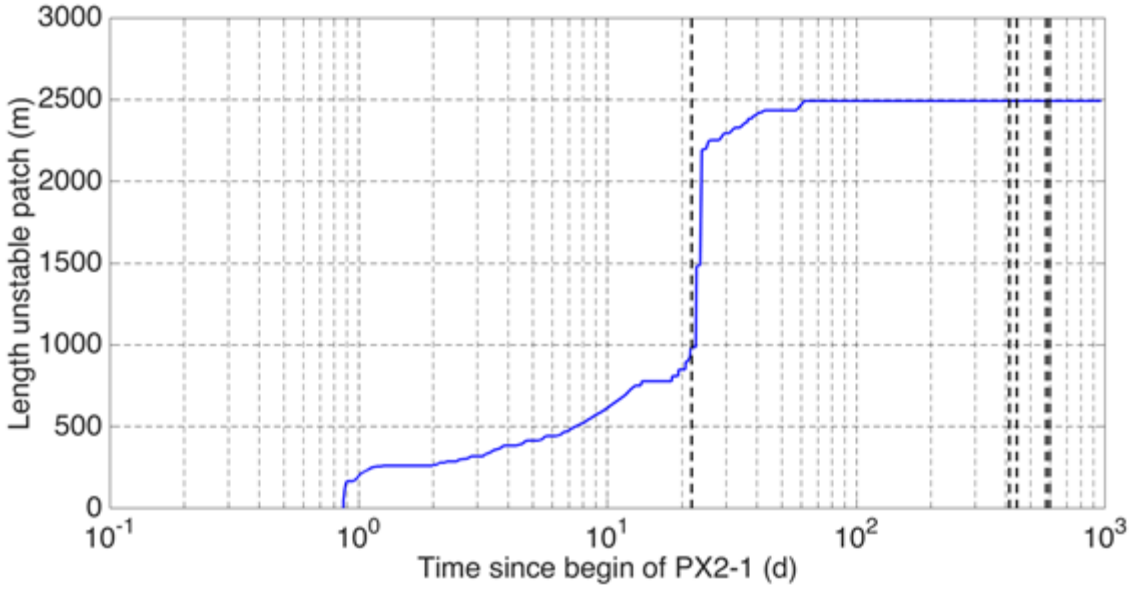

Figure 7: Temporal evolution of the maximum length of the unstable patch along the rupture plane. The vertical dashed lines depict the beginning and end of the three hydraulic stimulations. It is assumed that unstable segments during or after PX2-1 keep unstable. As such, the length depicted here is the maximum possible.

5. IMPACT OF INJECTION PRESSURE ON STABILITY

The impact of injection pressure is evaluated by comparing the outputs presented so far, which mimic the actual injection scheme at Pohang, with those of two additional simulations, in which only the injection boundary condition changes (Figure 8). The tested injection volumes are equal to 1/3 and 1/9 of the actually injected volume (Figure 8a), which leads to wellhead pressures of approximately 30 and 10 MPa, respectively (Figure 8b). The hydromechanical response at the rupture plane in terms of overpressure (Figure 8c) and variation of effective normal and shear stresses (Figures 8d and 8e) is also reduced by factors approximately equal to 3 and 9 because the problem is linear elastic. Correspondingly, instability (as measured by *CFS;* Figure 8f), is also reduced by the same factors because the rupture plane is assumed to be cohesionless. In fact, if injection pressures are reduced by a factor of 3, which corresponds to approximately the maximum injection pressure at Basel (Häring et al., 2008), unstable conditions at the rupture plane still occur during and shortly after the hydraulic stimulations. However, the maximum *CFS* is limited to 0.44 MPa during the second hydraulic stimulation, resulting in a more stable situation (*CFS* = 1.52 MPa with the actual 90 MPa injection pressure). The maximum *CFS* drops even more, to 0.07 MPa, when injection pressure is 10 MPa, which corresponds to, e.g., the French regulation (Gerard et al., 2006), and unstable conditions are limited to short time periods during the hydraulic stimulations only. In short, microseismic events would have been still detected at the rupture plane even using significantly smaller injection pressures. However, *CFS* drops from 0.03 MPa (unstable conditions with Δp_{inj} =90 MPa), to -0.05 and -0.1 MPa (stable conditions with Δp_{inj} =30 MPa and 10 MPa, respectively) at the time of the mainshock. The length of the unstable patch (Figure 9) strongly depends on injection pressure and drops from 2500 m to 295 m when the injection pressure is reduced from 90 to 30 MPa, and to 145 m when the maximum injection pressure is 10 MPa. Despite the rupture plane is still close to instability even reducing drastically the injection pressure (small but negative values of *CFS* depicting stability), such small unstable patches would have led to significantly lower post-injection magnitudes. Thus, we conclude that the strong post-injection seismicity at Pohang can be attributed to the very high-pressure fluid injections in PX2.

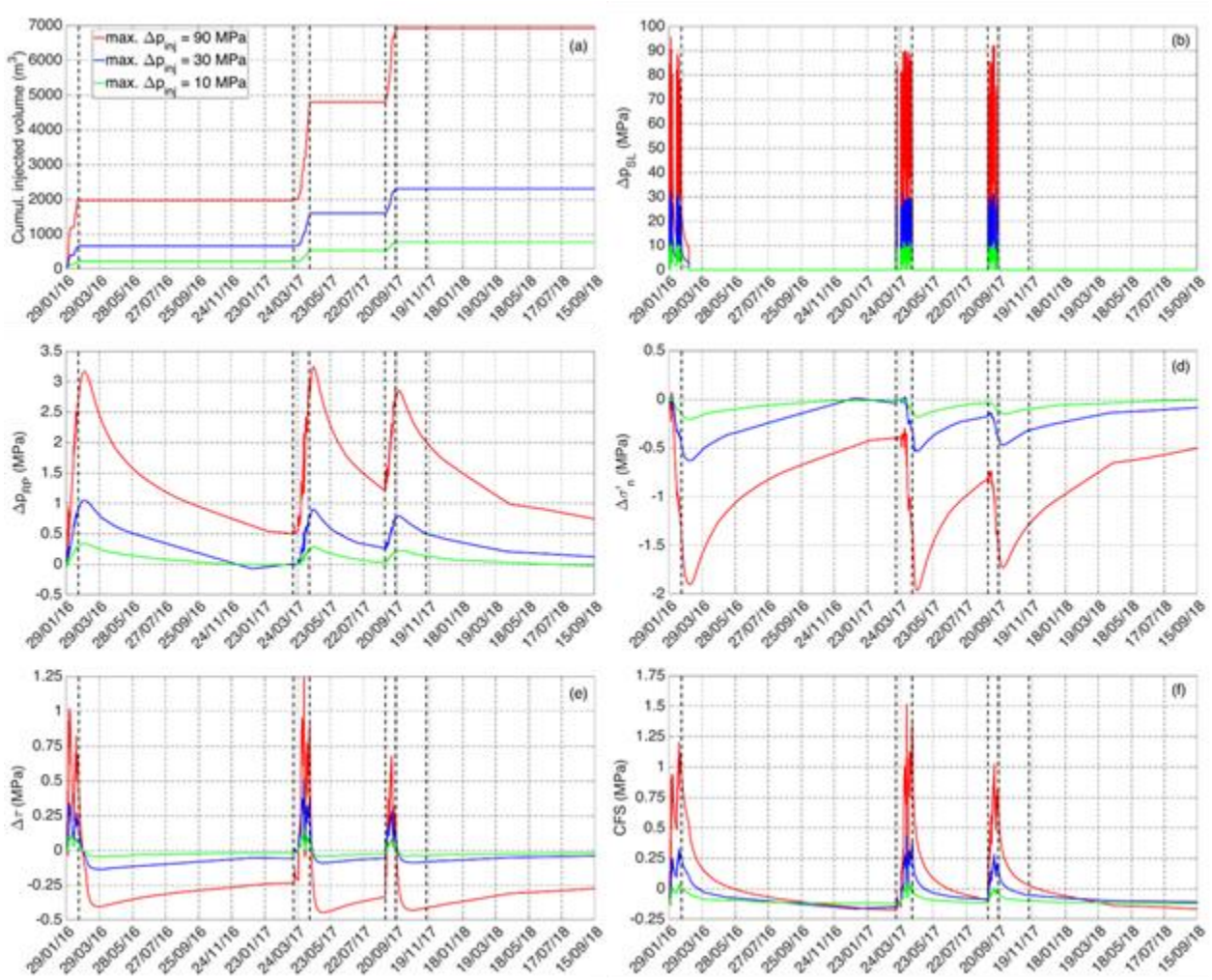

Figure 8: Impact of injection pressure on model outputs: (a) boundary conditions in terms of injected volume at the source layer; (b) overpressure at the source layer; (c) overpressure at the rupture plane; (d) variation of effective normal stress at the rupture plane; (e) variation of shear stress at the rupture plane; (f) CFS at the rupture plane. Note that panels (c) to (f) contain temporal evolution of variables at the central point of the rupture plane d_{OBS}=0.

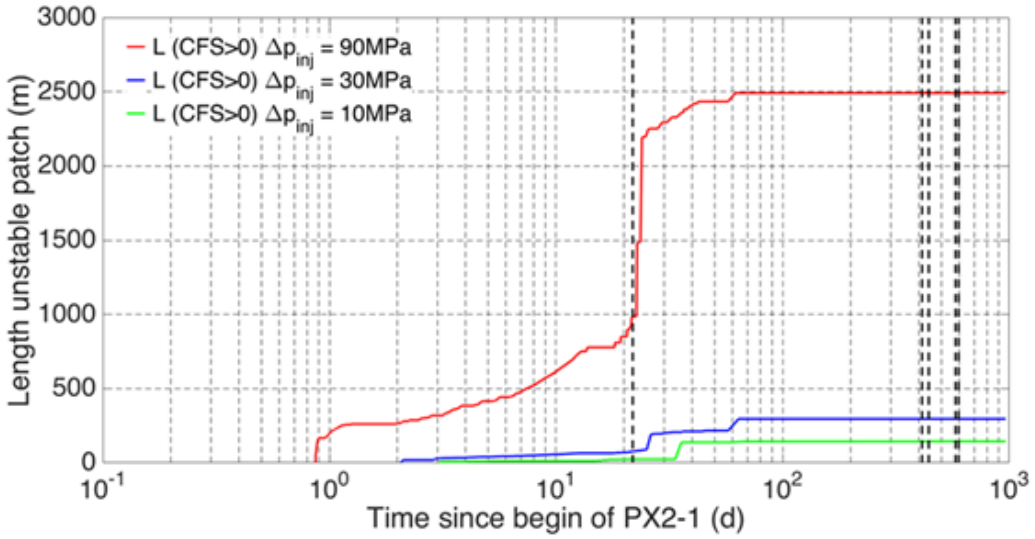

Figure 9: Temporal evolution of the length of the unstable patch for injection pressures Δp_{inj} = 90, 30 and 10 MPa.

6. CONCLUSIONS

We have analyzed the triggering mechanisms after the sequence of hydraulic stimulations in borehole PX2 at the EGS project at Pohang, South Korea. Special emphasis is placed on the instability conditions at the time of the M_w 5.5 mainshock on November 15, 2017, approximately two months after the cease of the last injection, located relatively far away from the injection source. To analyze the strong, delayed and migrated seismicity, a 2D hydromechanical model has been built. Our model represents one possible strong simplification of the real system. However, it is based on existing conceptual models of fault zone found in South Korea. The model reproduces the injection history well and forecasts unstable conditions at the rupture plane coherent with the monitored seismicity during and after the three hydraulic stimulations in borehole PX2. In fact, beyond model uncertainties (e.g., on the geometry, parameters, or even on the conceptual model), the model helps to understand the mechanisms triggering the seismicity at Pohang. The model has also been used to address the impact of different injection scenarios involving lower injection pressures at the same fault zone. Assuming that the model is just a simplification of the real system, and the validity of its hypothesis, our results indicate that:

- results are sensitive to the applied stress state and extremely sensitive to the friction coefficient. It has been observed that the system was critically stressed before the stimulation of the EGS.

- instability conditions at the rupture plane prevailed long after the end of injections. In particular, unstable conditions persisted along a ~2500 m-long patch at the rupture plane at the time of the M_w 5.5 mainshock and several months later, until August 2018. As such, the triggering of the mainshock can be attributed to the high injection pressures in borehole PX2.

- the model also reproduces unstable conditions right after the cease of each stimulation. However, the length of the unstable patch is relatively small (~800-1500 m) and would lead to a small event magnitude. Pressure diffusion after the last stimulation destabilizes a larger patch of ~2500 m, capable of yielding a large event magnitude. Thus, the long delay between the end of injection and the mainshock is attributed to pressure diffusion, also enhanced by poroelastic effects.

- model response is extremely sensitive to the applied injection pressure. Three models involving different injection pressures of 90 (base case reproducing in-situ conditions), 30 and 10 MPa have been compared. The results show that lowering the injection pressure leads to a dramatic alleviation of instability. In fact, lower injection pressures of 30 and 10 MPa lead to stable conditions at the rupture plane at the time of the mainshock, and to significantly smaller unstable patches (reduction from 2500 m to 100-300 m by reducing the injection rate by a factor of 3 to 9). This conclusion is particularly important for future stimulations of EGS, especially when critically stressed faults are present in the project area.

Acknowledgments

The work of the first two authors was supported by the European Union Horizon 2020 research and innovation programme under grant agreement number 691728, and by the Swiss State Secretariat for Education, Research and Innovation (SERI) under contract number 15-0316-1. The opinions expressed and arguments employed herein do not necessarily reflect the official views of the Swiss Government. Víctor Vilarrasa acknowledges funding from the European Research Council (ERC) under the European Union's Horizon 2020 Research and Innovation Programme through the Starting Grant GEoREST (www.georest.eu) (grant agreement No. 801809).

REFERENCES

Barth, N. C., Boulton, C. J., Carpenter, B. M, Batt, G. E. and Toy, V. G. (2013). Slip localization on the southern alpine Fault, New Zealand. *Tectonics*, 32: 620–640, doi:10.1002/tect.20041.

Bethmann, F., Ollinger, D., Tormann, Th. and Meier, M. P. Seismicity analysis with spatial or temporal relation to the deep geothermal project in Pohang, Korea. Submitted for publication in the *Proc. of the World geothermal Congress*, Reykjavik 2020.

Birsoy, Y.K. and Summers, W.K. (1980). Determination of aquifer parameters from step tests and intermittent pumping, Ground Water, vol. 18, no. 2, pp. 137-146.

Carrera, J., Alcolea, A., Medina, A., Hidalgo, J. and Slooten, L. J. (2005). "Inverse problem in hydrogeology." *Hydrogeology Journal*, 13: 206-222.

Castilla, R., Meier, P. M. and Alcolea, A. Integrated analysis of observations with spatial or temporal relation to the deep hydraulic stimulation project in Pohang during 2016/2017 -Stress State Analysis-. *Submitted to Geothermics*.

Choi, J-K., Yang, S-J., Han, S.R. and Kim, Y-S. (2015). Fault zone evolution during Cenozoic tectonic inversion in SE Korea, *Journal of Asian Earth Sciences*, 98: 167-177. https://doi.org/10.1016/j.jseaes.2014.11.009.

Dahm, T., Hainzl, S., Hofmann, H., Cesca, S., Zimmermann, G. and Huenges, E. (2018). Combining geomechanical modeling with physics-based seismicity models to assess the trigger probabilities of the Mw 5.5 2017 Pohang earthquake. Paper S23B-0518, *AGU Fall Meeting*, Washington D.C., 10-14 December 2018.

De Simone, S., Vilarrasa, V., Carrera, J., Alcolea, A. and Meier, P. (2013). Thermal coupling may control mechanical stability of geothermal reservoirs during cold water injection. *Physics and Chemistry of the Earth, Parts A/B/C*, 64:117-126.

De Simone, S., Carrera, J. and Vilarrasa, V. (2017). Superposition approach to understand triggering mechanisms of post-injection induced seismicity. *Geothermics* 70, 85-97.

Deichmann, N. and Giardini, D. (2009). Earthquakes Induced by the Stimulation of an Enhanced Geothermal System below Basel (Switzerland). *Seismological Research Letters*, 80(5): 784-798.

Deichmann, N., Kraft, T. and Evans, K. F. (2014). Identification of faults activated during the stimulation of the Basel geothermal project from cluster analysis and focal mechanisms of the larger magnitude events. *Geothermics*, 52: 84-97.

Dorbath, L., Cuenot, N., Genter, A. and Frogneux, M. (2009). Seismic response of the fractured and faulted granite of Soultz-sous-Forets (France) to 5 km deep massive water injections. *Geophys. J. Int*. (2009) 177, 653–675 doi: 10.1111/j.1365-246X.2009.04030.x

Eshelby, J.D. (1957). The determination of the elastic field of an ellipsoidal inclusion, and related problems, *Proc. R. Soc. Lond. A*,241(1226): 376–396.

Evans, K.F., Zappone, A., Kraft, T., Deichmann, N. and Moia, F. (2012). A survey of the induced seismic responses to fluid injection in geothermal and CO2 reservoirs in Europe. *Geothermics*, 41: 30-54. https://doi.org/10.1016/j.geothermics.2011.08.002.

Gerard, A., Genter, A., Kohl, T., Lutz, P., Rose, P. and Rummel, F. (2006). The deep EGS (enhanced geothermal system) project at Soultz-sous-Forêts (Alsace, France). Geothermics 35(5–6):473–483.

Grigoli, F., Cesca, S., Rinaldi, A. P., Manconi, A., López-Comino, J. A., Clinton, J. F., Westaway, R., Cauzzi, C. and Dahm, T. (2018). The November 2017 Mw 5.5 Pohang earthquake: A possible case of induced seismicity in South Korea. Science 360(6392): 1003-1006, doi: 10.1126/science.aat2010.

Häring, M.O., Schanz, U., Ladner, F. and Dyer, B.C. (2008). Characterisation of the Basel-1 Enhanced Geothermal System. *Geothermics* 37(5): 469-495. https://doi.org/10.1016/j.geothermics.2008.06.002.

Iio, Y. (1997). Frictional coefficient on faults in a seismogenic region inferred from earthquake mechanism solutions. *Journal of geophysical research*, 102(B3): 5403-5412.

KGC (2019). Summary Report of the Korean Government Commission on Relations between the 2017 Pohang Earthquake and EGS project. March 2019, 205 pages.

KIGAM (2018). Earthquake. Korean Institute of Geoscience and Mineral Resources, 64 pages.

Kim, K.-I., Min, K.-B., Kim, K.-Y., Choi, J. W., Yoon, K.-S., Yoon, W. S., Yoon, B., Lee, T. J. and Song, Y. (2018). Protocol for induced microseismicity in the first enhanced geothermal systems project in Pohang, Korea. *Renewable and Sustainable Energy Reviews*, 91:1182-1191. doi:10.1016/j.rser.2018.04.062

Kwon, S., Xie, L., Park, S., Kim, K.I., Min, K.B., Kim, K. Y., Zhuang, L., Choi, J., Kim, H. and Lee, T. J. (2019). Characterization of 4.2-km-Deep Fractured Granodiorite Cores from Pohang Geothermal Reservoir, Korea. Rock Mechanics and Rock Engineering,52(3): 771–782. Doi: 10.1007/s00603-018-1639-2.

Lay, T. and Wallace, T.C. (1995). Modern Global Seismology. *Academic Press*, ISBN #0-12-732870-X.

Lee, Y., Park, S., Kim, J., Kim, H. C. and Koo, M. H. (2010), Geothermal resource assessment in Korea. *Renewable and Sustainable Energy Reviews*, 14 (8), 2392-2400, doi:10.1016/j.rser. 2010.05.003.

Lee, T. J., Song, Y., Park, D. W., Jeon, J. and Yoon, W. S. (2015). Three dimensional geological model of Pohang EGS pilot site, Korea. *Proceedings of the World Geothermal Congress, Melbourne, Australia, 19-25 April 2015.*

Lim, H., Deng, K., Kim, Y., Ree, J-H. and Song, T-R. A. (2018). Mw 5.4 Pohang earthquake, South Korea and poroelastic stress change associated with fluid injection. Paper S23B-0522, *AGU Fall Meeting*, Washington D.C., 10-14 December 2018.

McClure, M. W. and Horne, R. N. (2012). The effect of fault zone development on induced seismicity. *Proc. 37th Workshop on Geothermal Reservoir Engineering*, Stanford University, SGP-TR-194.

Meier, P. M., Ollinger, D. and Alcolea, A. Analysis of the 3 days constant rate injection test in PX1 from December 17 to 20, 2016 with respect to an observed non-flow boundary conjectured to be low permeable fault core material extending laterally over several hundred meters almost perpendicular to the sub-vertical structure stimulated during the PX1-1 stimulation campaign. Submitted to *Geothermics.*

Min, K. B., Park, S., Xie, L., Kim, K. I., Yoo, H., Kim, K. Y., Choi, J., Yoon, K. S., Yoon, W. S., Lee, T. J. and Song, Y. (2017). Hydraulic Shearing and Hydraulic Jacking Observed during Hydraulic Stimulations in Fractured Geothermal Reservoir in Pohang, Korea. *American Geophysical Union, Fall Meeting 2017*, abstract #H23A-1630.

Milly, P.C.D. (1984). A mass-conservative procedure for time stepping in models of unsaturated flow. *Proceedings Fifth International Conference on Finite Elements in Water Resources*, Ed. J. P. Laible et al., Springer-Verlag, New York: 103-112.

Noda, H. and Lapusta, N. (2013). Stable creeping fault segments can become destructive as a result of dynamic weakening. *Nature* (493): 518-523.

Olivella, S., Carrera, J., Gens A. and Alonso, E. E. (1994). Non-isothermal Multiphase Flow of Brine and Gas through Saline media. *Transport in Porous Media*, 15, 271:293.

Olivella, S., Gens, A., Carrera, J. and Alonso, E. E., (1996), Numerical Formulation for a Simulator (CODE_BRIGHT) for the Coupled Analysis of Saline Media, *Engineering Computations*, 13(7): 87-112.

Reasenberg, P. A. and Simpson, R. W. (1992). Response of regional seismicity to the static stress change produced by the Loma Prieta earthquake, *Science*, 255 (5052), 1687-1690, doi:10.1126/science.255.5052.1687.

Renard, Ph. (2017). Hytool: an open source matlab toolbox for the interpretation of hydraulic tests using analytical solutions. *Journal of Open Source Software*, 2(19), 441, doi:10.21105/joss.00441

Segall, P. and Fitzgerald, S. (1998). A note on induced stress changes in hydrocarbon and geothermal reservoirs. *Tectonophysics*, 289(1-3): 117-128.

Son, M., Song, C. W., Kim, M. C., Cheon, Y., Cho, H. and Sohn, Y. K. (2015). Miocene tectonic evolution of the basins and fault systems, SE Korea: dextral, simple shear during the East Sea (Sea of Japan) opening, *Journal of the Geological Society*, 172 (5), 664-680, doi:10.1144/jgs2014-079.

Stober, I. (2011). Depth and pressure dependent permeability in the upper continental crust: data from the Urach 3 geothermal borehole, southwest Germany. *Hydrogeology Journal* 19: 685:699.

Stober, I. and Bucher, K. (2007). Hydraulic properties of the crystalline basement. *Hydrogeology Journal* 15: 213–224 doi 10.1007/s10040-006-0094-4.

Stober, I. and Bucher, K. (2015). Hydraulic conductivity of fractured upper crust: insights from hydraulic tests in boreholes and fluid-rock interaction in crystalline basement rocks. *Geofluids* 15: 161-178. doi: 10.1111/gfl.12104.

Tanikawa, W. and Shimamoto, T. (2009). Frictional and transport properties of the Chelungpu fault from shallow borehole data and their correlation with seismic behavior during the 1999 Chi-Chi earthquake. Journal of Geophysical Research, 114, B01402, doi:10.1029/2008JB005750.

Theis, C. V. (1935). The relation between the lowering of the piezometric surface and the rate and duration of discharge of a well using groundwater storage, *Am. Geophys. Union Trans.*, vol. 16, pp. 519-524.

Yoo, H., Park, S., Xie, L., Min, K-B., Rutqvist, J. and Rinaldi, A. P. (2017). Numerical Modeling of Coupled Hydromechanical Behavior of Fractured Geothermal Reservoir at Pohang Enhanced Geothermal System (EGS) Site. In: *Proc. 4th ISRM Young Scholars Symposium on Rock Mechanics, 10-13 May, Jeju, Korea, International Society for Rock Mechanics and Rock Engineering*.

Yoo, H. (2018). Numerical modeling of hydraulic stimulation at a fractured geothermal reservoir. *M.Sc. Thesis.* Seoul National University, 99 pages.

Zingg, O., Alcolea, A., Castilla, R. and Meier, P. M. Geology and geophysics in Pohang. Submitted to *Geothermics*.